Article

Time-domain signatures of distinct correlated insulators in a moiré superlattice

Eric A. Arsenault [1], Yiliu Li[1], Birui Yang [2], Takashi Taniguchi [3], Kenji Watanabe [4], James C. Hone [5], Cory R. Dean [2], Xiaodong Xu[6] & X.-Y. Zhu [1]✉

Among expanding discoveries of quantum phases in moiré superlattices, correlated insulators stand out as both the most stable and most commonly observed. Despite the central importance of these states in moiré physics, little is known about their underlying nature. Here, we use pump-probe spectroscopy to show distinct time-domain signatures of correlated insulators at fillings of one ($v = -1$) and two ($v = -2$) holes per moiré unit cell in the angle-aligned WSe_2/WS_2 system. Following photo-doping, we find that the disordering time of the $v = -1$ state is independent of excitation density (n_{ex}), as expected from the characteristic phonon response time associated with a polaronic state. In contrast, the disordering time of the $v = -2$ state scales with $1/\sqrt{n_{ex}}$, in agreement with plasmonic screening from free holons and doublons. These states display disparate reordering behavior dominated either by first order ($v = -1$) or second order ($v = -2$) recombination, suggesting the presence of Hubbard excitons and free carrier-like holons/doublons, respectively. Our work delineates the roles of electron–phonon (e–ph) versus electron–electron (e–e) interactions in correlated insulators on the moiré landscape and establishes non-equilibrium responses as mechanistic signatures for distinguishing and discovering quantum phases.

Moiré materials offer unprecedented and highly tunable platforms for understanding the emergence of quantum phases of matter and for exploring future device applications. Among the quantum phases realized in these systems, the correlated insulators stand out as the most commonly observed[1–15]. Other quantum phases, including mixed bosonic-fermionic states[16–18], superconductors[19,20], and various quantum Hall states[21–28], are often directly related to or appear in the vicinity of correlated insulators. Despite the obvious importance of correlated insulators in moiré systems, an understanding of the hierarchy of stabilizing/destabilizing interactions remains largely limited to a reliance on simple models, such as the Hubbard Hamiltonian[29,30].

Establishing how correlated insulators differ mechanistically is essential to understanding their properties, such as varying critical temperatures (T_c), and connections to other quantum phases. We focus on the most robust quantum states discovered to date at moiré interfaces—correlated insulators at integer filling factors of moiré superlattices in transition metal dichalcogenide heterobilayers[2–15]. We choose the angle-aligned WSe_2/WS_2 moiré system, where the $v = -1$ and $v = -2$ correlated insulator states exhibit high T_c of ~150 K and ~80 K, respectively[2,3,6,8,11]. Recently, we suggested that the observed high T_c is, in addition to many-body e–e interactions, related to polaronic stabilization due to e–ph interactions[31].

[1]Department of Chemistry, Columbia University, New York, NY, USA. [2]Department of Physics, Columbia University, New York, NY, USA. [3]Research Center for Materials Nanoarchitectonics, National Institute for Materials Science, Tsukuba, Japan. [4]Research Center for Electronic and Optical Materials, National Institute for Materials Science, Tsukuba, Japan. [5]Department of Mechanical Engineering, Columbia University, New York, NY, USA. [6]Department of Physics, University of Washington, Seattle, WA, USA. ✉e-mail: xz2324@columbia.edu

In the angle-aligned WSe_2/WS_2 moiré system studied here, there are two potential wells at high symmetry points in each moiré unit cell, leading to the formation of two narrow moiré bands[32,33]. Recently, this was experimentally confirmed by Park et al. via reflective magnetic circular dichroism measurements[16]. At half filling ($\nu = -1$) of the first moiré band (lower energy), many-body correlation results in gap opening near the top of the valence band and the formation of an upper and a lower Hubbard band (UHB and LHB, respectively). The second moiré band is believed to be located within the Hubbard gap of the first moiré band and the $\nu = -1$ correlated insulator is properly called a charge-transfer (CT) insulator[32] instead of a Mott insulator[34]. At $\nu = -2$, the inter-band Coulomb energy (U', rather than the intra-band Coulomb energy, U) favors the half filling of both bands and the result is a two-band Mott insulator[16] rather than a trivial band insulator[6]. To understand these correlated insulators, we take a time-domain approach[31] in which a pump pulse creates holons and doublons across the correlated gap and a probe pulse detects the disordering dynamics[35] via exciton sensing of the dielectric environment[2,3,6,8]. Such an approach directly accesses the timescales relevant to electronic or atomic motions that are not accessible in steady-state spectroscopy or transport measurements. In particular, disordering of a correlated state occurs on a timescale of the characteristic system response, linked to either electron hopping or the oscillation period of a relevant phonon mode, depending on whether e–e or e–ph interactions play the dominate role in stabilizing the state[36]. Here, we apply such an approach coupled with fluence-dependent measurements. Through this lens, we map the mechanistic regimes governing correlated insulator stability/instability in moiré systems as a function of photoexcitation density, n_{ex}.

Results and discussion

Steady-state and transient correlated state sensing

Figure 1a illustrates the WSe_2/WS_2 heterostructure (AB stacked, $\theta = 60 \pm 1°$) featuring top and bottom gates, each consisting of a hexagonal boron nitride (h-BN) dielectric spacer and a few-layer graphene (Gr) electrode. The dual-gate structure allows either hole ($\nu < 0$) or electron ($\nu > 0$) doping from an applied gate voltage (V_g), while the electric field at the moiré interface can be maintained at zero. Figure 1b illustrates the static reflectance spectrum of the device as a function of V_g and moiré filling factor ν (defined here as charge filling per moiré unit cell). In the reflectance measurement, the excitonic oscillator strength, sensitive to changes in the dielectric environment, is an effective probe of correlated state formation. We choose the lowest energy moiré exciton of WSe_2 as our dielectric sensor for its high oscillator strength and therefore high sensitivity. At $\nu = \pm 1, \pm 2$, we observe an increased exciton signal as the effective dielectric constant decreases upon the formation of correlated insulator states[2,3,6,8]. Further device characterization can be found in Supplementary Fig. 1.

By introducing pulsed laser excitation (and detection), we can further perform transient reflectance measurements on the same device architecture[31]. This allows us to obtain both time-resolved and gate-dependent reflectance spectra (see Supplementary Figs. 2–3). For excitation, we employ a pump with photon energy (1.55 eV) below the optical gaps of WSe_2 and WS_2 to uniquely target the correlated states. This avoids pump-induced interlayer exciton formation which would result in long-lived responses on the nanosecond time scale[33]. The absorption of a pump photon excites a hole from the LHB of the correlated insulator deep into the valence band(s). The excited holes relax within this continuous manifold on ultrafast time scales, typically of the order of 10s–100s femtoseconds due to scattering with other
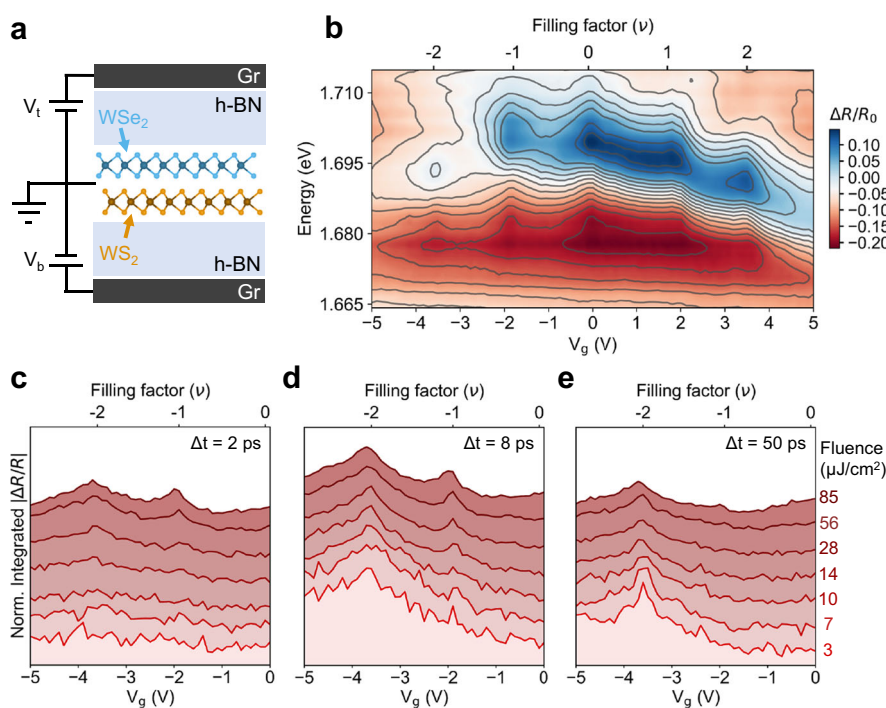

Fig. 1 | Steady-state and transient correlated state detection via exciton sensing. a Schematic of device architecture where the WSe_2/WS_2 heterobilayer is symmetrically encapsulated by top and bottom gates (V_t and V_b, respectively) consisting of hexagonal boron nitride (h-BN) and few-layer graphene (Gr). **b** Gated ($V_g = V_t = V_b$) steady-state reflectance spectrum of the lowest energy moiré exciton of WSe_2. Here, $\Delta R = R - R_0$ where R is the reflected signal from the bilayer and dual gate region while R_0 is the reflected signal from a region with gates and no bilayer. **c**–**e** Gated ($V_g = V_t = V_b$) transient reflectance response as a function of pump

fluence at $\Delta t = 2, 8, 50$ ps, respectively. Shown is the integrated response centralized around the lowest energy WSe_2 moiré exciton sensor. The different fluence-dependent responses have been offset and multiplied by -1 for clarity. Associated fluence labels are shown on the side of panel e and are consistently colored throughout the other panels. Here, $\Delta R = R_{on} - R_{off}$ where the subscript indicates either pump-on or -off spectra. See Methods for further details. All data were collected at 11 K.
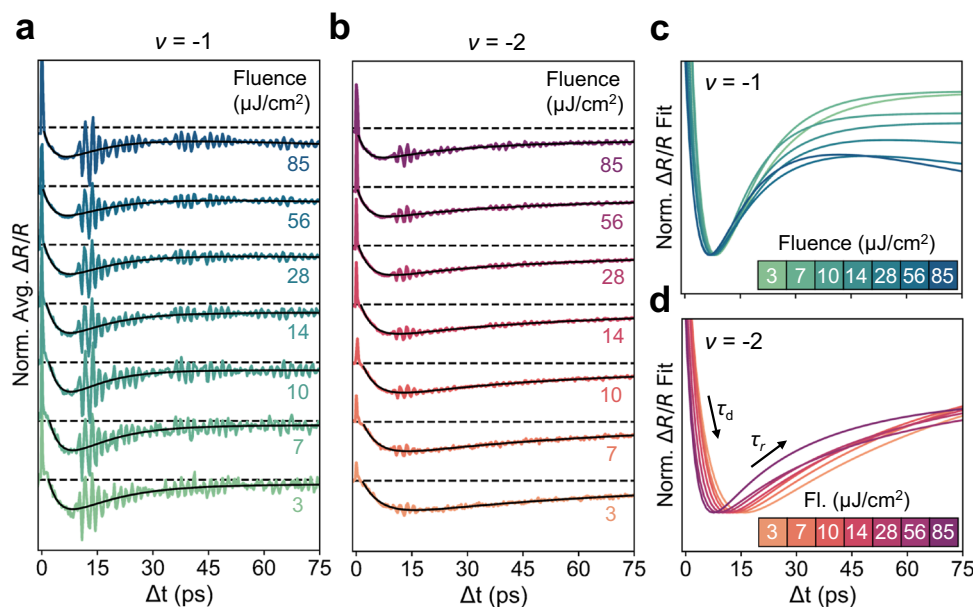
Fig. 2 | Non-equilibrium correlated insulator response. a, b Fluence-dependent temporal response of the $v = -1$, -2 states, respectively. The time traces were averaged in a narrow window about the maximum of the lowest energy WSe$_2$ moiré exciton sensor. Each fluence-dependent transient has been normalized for clear comparison of the dynamical response (see Supplementary Fig. 7 for unnormalized data where the overall signal trend is preserved). Data are shown in shaded colors while the fits used for time constant extraction are shown in black. See the Methods section for further details. Throughout the panels, increasing pump fluence is shown from light to dark shades. All fluence-dependent data are colored consistently for each of the filling factors throughout the figure. All data were collected at 11 K. **c, d** To more easily and directly visualize the trends in the fluence-dependent dynamics (without the substantial interlayer phonon response), the normalized fits from (**a, b**) are shown in (**c, d**), respectively. Arrows indicating the time constants associated with the disordering dynamics (τ_d) and recovery dynamics (τ_r) are labeled in (**d**).

carriers and optical phonons[37], towards the upper unoccupied band(s) (the UHB or the CT band)[32]. The result is the formation of holon-doublon pairs across the correlation gap (see Supplementary Fig. 4 for schematic). The presence of holons and doublons leads to disordering of the correlated insulator on characteristic timescales determined by e–e or e–ph interactions[36]. Recovery of the charge order reaches the so-called "bottleneck" on a timescale determined by recombination of holons and doublons across the gap[35]. The timescale of disordering is captured by the transient increase in the effective dielectric constant, monitored through the exciton sensor covered by a probe pulse centered at 1.65 eV (spanning the lowest energy moiré exciton of WSe$_2$). We note that in the current measurements, we focus on the hole doping side because our transient measurements are most sensitive to the correlated states which reside exclusively in the same layer as the WSe$_2$ excitonic sensor due to the type-II band alignment at the WSe$_2$/WS$_2$ interface[2,3]. Correlated state recovery is tracked through the subsequent reduction in the effective dielectric constant as the original insulator behavior reemerges.

Figure 1c–e show transient reflectance spectra integrated around the lowest energy moiré transition of WSe$_2$ as functions of both applied gate voltage, V$_g$, and pump-probe time delay, Δt, at varying pump fluences. The pump fluence is increased until saturating behavior is reached in the transient response (Supplementary Fig. 5). In agreement with the static reflectance spectra, correlated state responses at $v = -1$, -2 are observed in the time-resolved spectra, with the maximum response (disordering) in a few ps and recovery (reordering) in tens of ps. With increasing fluence, the magnitude of the correlated state response also increases. Intriguingly, the response of the $v = -2$ state to pump-induced disordering occurs in a broader V$_g$ range than the $v = -1$ state does (Fig. 1c–e), in contrast to the steady-state measurement (Fig. 1b). This may suggest that the transient measurements are particularly sensitive to an expanse of otherwise hidden states with varying charge ordering around $v = -2$, as predicted for lower filling factors[38,39]. In the present case, the magnitude of the

transient response around $v = -2$ indicates a significant change in the dielectric environment and therefore a substantial non-equilibrium photoinduced response. The states in this region also appear to have varying recovery timescales (Fig. 1e) which can be seen as a narrowing in the transient response along the V$_g$ axis at later Δt, particularly at lower pump fluence. In the following, we focus on the disordering and reordering dynamics at $v = -1$, -2.

Distinct temporal responses of correlated insulator states
Figure 2a, b show the transient reflectance responses of the $v = -1$, -2 states for the indicated pump fluences ($f = 3$–$85\,\mu$J/cm^2). Following the coherent artifact arising from pump-probe overlap at $\Delta t = 0$ ps, the non-equilibrium response of the correlated states is initially related to disordering of the equilibrium charge configuration, as evidenced by an increase in the effective dielectric constant detected through bleaching of the exciton transition. In each case, the disordering reaches a maximum magnitude after a few ps and subsequently recovers. The black solid curve in each case is a fit consisting of a single exponential decay (disordering) and either a single exponential first order ($v = -1$) or a second order ($v = -2$) recovery (reordering); further fit details can be found in the Methods section (fit residuals shown in Supplementary Fig. 6 and unnormalized data and fits in Supplementary Fig. 7). The chosen functional form for the recovery dynamics will be explicitly discussed further below. Finally, an additional offset is also included to account for the much longer timescale (»100 ps) recovery dynamics. This offset is negligible at low excitation fluence but becomes significant at $f > 14\,\mu$J/cm^2. As detailed in control experiments on the undoped charge neutral state ($v = 0$, Supplementary Fig. 8) the long-lived offset can be attributed to hole injection into the WSe$_2$/WS$_2$ moiré structure from thermionic emission of hot electrons in the unavoidably photo-excited Gr electrodes at sufficiently high excitation densities (Supplementary Fig. 9)[40,41]. Concomitant with the dynamic responses from disordering and recovery are temporal oscillations of interlayer phonon modes which have been discussed
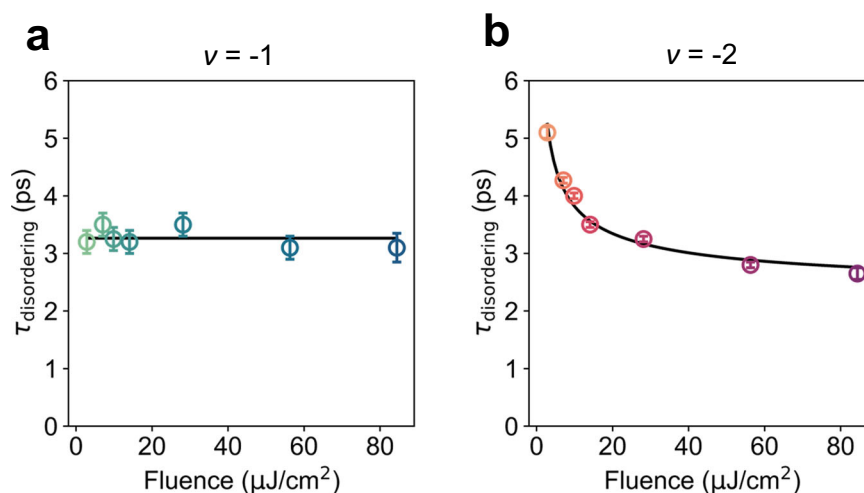
Fig. 3 | Disordering in the polaronic versus plasmonic limits. a Disordering time constant (τ_d) for $v = -1$ as a function of fluence. The linear fit trend line is shown in black. **b** Disordering time constant (τ_d) for $v = -2$ as a function of fluence. Shown in black is the fit of the form $\propto 1/\sqrt{n_{ex}} + \tau_{const}$. Throughout the figure, all error bars indicate 99% confidence intervals. Large circle outlines have been added to aid with data visualization. The fluence-dependent shaded colors for the $v = -1$, -2 states are consistent with the data shown elsewhere in the text. See the Methods section for further details.

elsewhere[42]. These modes are coherent phonon wavepackets launched from strain fields induced by the pump at the Gr electrodes. These wavepackets propagate through the h-BN prior to impinging on the heterobilayer with an apparent delay as determined by the phonon group velocity.

To more clearly view the disordering and recovery dynamics without interference from the coherent phonon oscillations, we replot the normalized fits independently from the data in Fig. 2c, d for $v = -1$, -2, respectively. The disordering and recover dynamics of the $v = -1$ state are found to be independent of fluence in the entire investigated range ($f = 3$–$85 \, \mu J/cm^2$). In contrast, the $v = -2$ state exhibits distinct behavior—both the disordering and the recovery accelerate with increasing fluence. To quantitatively compare the two correlated insulator states, we plot in Fig. 3a, b the disordering time (τ_d) for the at $v = -1$ and -2 states, respectively, as functions of fluence.

For the $v = -1$ state, disordering occurs with a time constant $\tau_d = 3.3 \pm 0.2$ ps, independent of the photoexcited carrier density, n_{ex}, of the correlated insulator (up to saturation of the observed transient response in the investigated pump fluence range). This result precludes a pure electronically-driven disordering mechanism, the rate ($= 1/\tau_d$) of which should increase with n_{ex} due to carrier screening of the many-body electronic interactions. Instead, the constant τ_d suggests a time scale characteristic of e–ph interactions and rate-limited by the oscillation period of the relevant phonon mode(s), often described as the amplitude mode in charge density wave (CDW) systems[36,43]. Our initial pump-probe measurements on the $v = -1$ correlated insulator state in the WSe_2/WS_2 moiré superlattice revealed thermal activation behavior in the disordering process, suggesting the polaronic nature of the correlated insulator, in agreement with an ab initio calculation[31]. The independence of disordering rate on n_{ex} observed here not only confirms the polaronic interpretation, but also reveals the dominance of e–ph interactions in stabilizing the charge order in the $v = -1$ correlated insulator. Such a polaronic and ordered correlated state is similar to a CDW state[44]; however, unambiguous delineation between Mott insulators versus CDW ordering remains a subject of discussion[45].

The observed τ_d can be understood as relating to the oscillation period (typically taken as either a half or quarter period) of phonon mode(s) involved, as shown in the related CDW systems[36,43]. The corresponding mode frequency is consistent with the fact that the moiré deformation potential likely involves acoustic phonons accessible via

the momentum range defined by the mini-Brillouin zone of the moiré superlattice[31]. Interestingly, in the fit residuals, a low frequency oscillation attributable to this phonon mode is potentially present at $\Delta t <$ 10 ps; however, this remains speculative as this feature is obscured by the interlayer modes after only a single period (Supplementary Fig. 6). Further suggestive, this behavior is noticeably absent in the control $v = 0$ data (Supplementary Fig. 8).

In stark contrast to the behavior of the $v = -1$ state, the disordering time, τ_d, for the $v = -2$ state displays a strong dependence on fluence (Fig. 3b). This is unexplainable by only consiring e–ph interactions and instead suggests the importance of many-body electronic interactions. In particular, we find that the disordering time can be well-described by the functional form $\tau_d \propto 1/\sqrt{n_{ex}} + \tau_{const}$ (solid black curve in Fig. 3b). The square root dependence on doping density is well-known for the 2D plasmon frequency[36,43]. In other words, disordering as a result of photoexcited carrier screening occurs on a characteristic timescale inversely proportional to the plasmon frequency, ω_p[36], as reported for the ultrafast collapse of order in the excitonic insulator $1T$-$TiSe_2$[43]. We conclude that disordering of the $v = -2$ correlated insulator at the WSe_2/WS_2 moiré interface observed here is determined by the electronic response, namely screening by photodoped holons and doublons. Our previous measurement on temperature-dependent disordering of the $v = -2$ state shows a thermal activation energy lower than that of the $v = -1$ state[31]. The current result, in combination with our previous finding, reveals that plasmonic screening overwhelms polaronic stabilization in the disordering of the $v = -2$ correlated insulator. We note that, while the observed τ_d is dominated by screening as shown by the $1/\sqrt{n_{ex}}$ dependence, there seems to be a fundamental limit to τ_d as captured by the offset, $\tau_{const} = 2.2 \pm 0.1$ ps. The exact origin of this offset is not known, but we speculate it may be associated with either additional e–ph interactions[31] or a deviation from the pure 2D plasmon response in the moiré superlattice[46]. Papaj and Lewandowski recently theoretically proposed that the coupling of charge order to the collective plasmon response can result in plasmon band folding and gap opening, leading to an upper bound in the plasmon frequency[46]. These issues deserve further investigations.

The fundamental distinction between the $v = -2$ and $v = -1$ insulator states can be understood from the difference in charge occupation of each moiré unit cell. In the $v = -2$ state, there are two holes (on two different sites) within each moiré unit, giving rise to the Coulomb
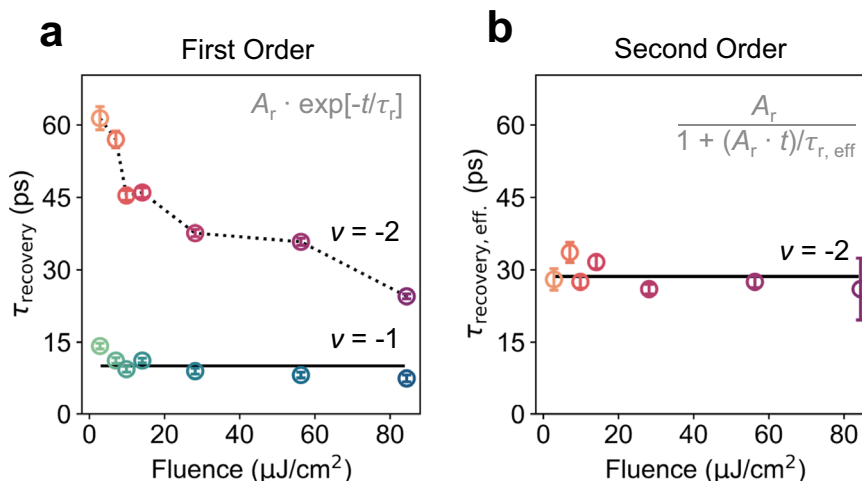
Fig. 4 | Charge reordering of distinct correlated insulators. a Reordering time constant (τ_r) for $\nu = -1$ and $\nu = -2$ as a function of fluence. Here, τ_r was extracted based on considering the recovery as a first order process (mono-exponential functional form, inset in **a**). The black line for $\nu = -1$ shows the linear fit trend line for τ_r as a function of fluence. The dotted black line for $\nu = -2$ shows the linear interpolation between data points to highlight the data trend. **b** Effective reordering time constant ($\tau_{r,\,eff}$) for $\nu = -2$ as a function of fluence. Here, $\tau_{r,\,eff}$ was extracted based on considering the recovery for $\nu = -2$ as a second order process (inset in **b**). The black line shows the linear fit for $\tau_{r,\,eff}$ as a function of fluence. Throughout the figure, all error bars indicate 99% confidence intervals. Large circle outlines have been added to aid with data visualization. The fluence-dependent shaded colors for the $\nu = -1, -2$ states are consistent with the data shown elsewhere in the text. See the Methods section for further details and Supplementary Fig. 10 for plots of k_r ($= 1/\tau_r$).

repulsion energy U'. For comparison, U' is absent for the $\nu = -1$ state where the second site remains unoccupied. The magnitude of U' (on the order of 50–100 meV)[16,32] dominates over the polaron stabilization energy (-13 meV estimated from thermal activation)[31]. As a result, photodoping of the two-band correlated insulator, $\nu = -2$, leads to a free carrier-like plasmonic response. In contrast, the stronger polaronic localization for the $\nu = -1$ state diminishes the collective plasmon character for holons and doublons.

The fundamental distinction between $\nu = -1$ and $\nu = -2$ is also reflected in the recovery dynamics, which are determined by holon-doublon recombination across the correlation gap[35]. Figure 4a shows the reordering time constants obtained from single exponential fits to the recovery component of the data in Fig. 2. For the $\nu = -1$ state, the reordering is captured as a first order process implied in the mono-exponential fit and verified by the approximate independence of recovery time constants τ_r on n_{ex}. Such a first-order kinetic process reveals that recombination of the perturbed $\nu = -1$ state derives from a "single body", i.e., a local holon-doublon pair called a Hubbard exciton[47]. This local holon-doublon pair is fortified by polaronic stabilization, which inhibits their separation into a free holon and a free doublon.

However, for $\nu = -2$, the single-exponential recovery time constant τ_r decreases with n_{ex}, indicating the failure of the first order kinetic model and that the recovery process is of higher order in n_{ex} (see Supplementary Fig. 10a). We find that the recovery for $\nu = -2$ is second order, i.e., the recovery rate is proportional to n_{ex}^2. To fit the recovery to a second order kinetic scheme, we use the functional form $A_r/(1 + A_r \cdot t/\tau_{r,\,eff})$, where A_r is a constant proportional to $n_{ex}^{(0)}$, the initial concentration of photo-excitation as controlled via the pump fluence. Figure 4b shows the resulting effective second order recovery time constant, $\tau_{r,\,eff}$, which is correctly n_{ex}-independent (see Supplementary Fig. 10b). The apparent second order process supports the two-body recombination kinetics of a holon and a doublon, in excellent agreement with the free-carrier nature of photo-doping of the $\nu = -2$ correlated insulator state.

In summary, we find distinct disordering and reordering mechanisms for the $\nu = -1$ and -2 states in the WSe$_2$/WS$_2$ moiré superlattice. The non-equilibrium response of the $\nu = -1$ state reveals its dominant polaronic nature, leading to disordering determined by a characteristic phonon time and re-ordering by the first-order recombination of a localized holon-doublon pair. In contrast, in the $\nu = -2$ state, e–e interactions dominate over e–ph interactions. As a result, photodoping of the $\nu = -2$ state results in free carrier-like holons and doublons, leading to disordering dominated by carrier screening and re-ordering dominated by second-order recombination of free holons and free doublons. The distinct non-equilibrium responses of the two correlated states define the richness of behavior accessible by a time-domain view. While we do possess sufficient sensitivity in the experiments presented here to resolve the correlated insulators at fractional filling of the moiré superlattice[6,8], further improvement in signal-to-noise ratio may allow us to resolve these states at fractional fillings and reveal their distinct dynamics. This remains a key objective of our research program on time-domain views of moiré quantum matter. Overall, the delicate balance or competition between e–e and e–ph interactions may provide an additional angle in understanding and ultimately controlling quantum phases on the moiré landscape or even in realizing otherwise hidden metastable phases.

Methods

60° device fabrication and gating

The WSe$_2$ and WS$_2$ monolayers are mechanically exfoliated from flux-grown bulk WSe$_2$ crystals and commercially purchased bulk WS$_2$ crystals (HQ Graphene), respectively. Prior to transfer, the crystal orientation of WSe$_2$ and WS$_2$ monolayers are first determined via polarization-resolved second harmonic generation (P-SHG). The monolayers are then stacked together by a dry-transfer technique with a polycarbonate stamp. To distinguish between R- and H-stacked configurations, P-SHG is again applied to the heterobilayer region after the device is fabricated, with results compared to individual monolayers. The error bars for the angle determination are well within $\pm 1°$. The sample is grounded via Gr contacts connected to the heterobilayer and single crystal h-BN dielectrics and Gr gates are used to encapsulate the device and provide control of the carrier density and displacement field (if desired) via external source meters (Keithly 2400). SF6 radio-frequency plasma is applied to the stack to etch the encapsulating h-BN and create connection to the Gr gates contacts. All electrodes are

defined with electron beam lithography and made of a three-layer metal film of Cr/Pd/Au (3 nm/17 nm/60 nm).

Spectroscopic measurements

For the spectroscopic measurements, the sample is cooled down to $T = 11$ K under vacuum ($<10^{-6}$ torr) with a closed-cycle liquid helium cryostat (Fusion X-Plane, Montana Instruments). We note that no laser-induced continuous heating was observed at any of the employed pump fluences. Steady-state reflectance measurements are carried out with a 3200 K halogen lamp (KLS EKE/AL). A 715 nm low pass filter is employed to avoid potential photodoping effects. Following collimation, the lamp light is focused onto the sample/substrate with a 100X, 0.75 NA objective. The reflected light is collected by the same objective and then dispersed with a spectrometer onto an InGaAs array (PyLoN-IR, Princeton Instruments). The steady-state reflectance spectrum is obtained by contrasting the reflected signal from the sample (R), which includes the bilayer and dual gate region, and the effective substrate (R_0), which includes a region with gates and no bilayer as follows: (R-R_0)/R_0. For the spatially-resolved reflectance experiments used for mapping of the bilayer, a dual-axis galvo mirror scanning system is employed[48]. Following spatial scanning of the sample as controlled via the angles of the galvo mirrors, the reflected light is spatially filtered through a pinhole and collected by the detector.

The steady-state photoluminescence (PL) experiments are performed with a HeNe laser (Model 31-2140-000, Coherent). The excitation power is set to the range 50–100 nW and focused onto the sample. The PL signal was spectrally filtered from the laser using a long-pass filter prior to dispersal with a spectrometer and detection (the same detection system described above is employed here).

The pump-probe experiments are seeded by femtosecond pulses (250 kHz, 1.55 eV, 100 fs) generated by a Ti:sapphire oscillator (Mira 900, Coherent) and regenerative amplifier (RegA 9050, Coherent). The output is then split to form the pump and probe arms. For the probe, a fraction of the fundamental is focused into a sapphire crystal to generate a white light continuum which is then spectrally filtered (750 ± 40 nm band pass filter) to cover the lowest energy WSe$_2$ moiré exciton. The pump beam (800 nm, fundamental) is then directed towards a motorized delay stage to control the time delay, Δt, and passed through an optical chopper to generate pump-on and -off signals. Following this, the pump and probe arms are directed collinearly to the sample through an objective (100X, 0.75 NA). The pump and probe spot diameters are ~2.36 μm and ~0.9 μm, respectively. Due temporal broadening from the objective, our instrument response function is ~200 fs. The same objective is used to collect the reflected light which is spectrally filtered to remove the pump and dispersed onto an InGaAs detector array (PyLoN-IR, Princeton Instruments). The pump-on and -off spectra at varying Δt are then used to calculate the transient reflectance signal ($\Delta R/R$) where $\Delta R = R_{on} - R_{off}$ with the subscript indicates either pump-on or -off spectra.

Assignment of filling factors

The charge density, n, in the WSe$_2$/WS$_2$ heterostructure, controlled by the applied gate voltages (V_t and V_b for the top and bottom gates, respectively), is determined using the parallel-plate capacitor model: $n = \frac{\varepsilon \varepsilon_0 \Delta V_t}{d_t} + \frac{\varepsilon \varepsilon_0 \Delta V_b}{d_b}$, where $\varepsilon \approx 3$ is the out-of-plane dielectric constant of hBN, ε_0 is the permittivity of free space, ΔV_i is the applied gate voltage relative to the valence/conduction band edge, and d_i is the thickness of the hBN spacer. The moiré density, n_O, is determined based on the moiré lattice constant, a_M, and is given by $n_0 = \frac{2}{\sqrt{3} a_M^2}$. The filling factor, υ, estimated as the ratio between the charge doping and moiré densities, is fit based on the experimental gate-dependent steady-state reflectance and photoluminescence measurements (Fig. 1b and Supplementary Fig. 1b). For the 60° device, the thickness of the top and

bottom hBN spacers is determined to be $d_t \approx 36.4$ and $d_b \approx 39.6$ nm, respectively. The twist angle is determined to be -0.8°.

Data analysis

In the following we describe the data processing involved in analyzing both the overall transient signal and the disordering/recovery dynamics. The data is first collected as a function of probe energy and pump-probe delay, Δt, at varying V_g and pump fluence. To generate Supplementary Fig. 2–3, pump-probe spectra are collected at a series of Δt at varying V_g and pump fluence. At each Δt and for each fluence, the V_g-dependent spectra are then combined as a function of probe energy versus V_g to generate two-dimensional pseudo-color plots. We take $V_g = V_t = V_b$ unless otherwise specified. The data from these plots are then integrated in the range 1.67–1.69 eV about the maximum of the lowest energy WSe$_2$ moiré sensor, normalized, offset, and multiplied by -1 to generate Fig. 1c–e.

To analyze the time traces, the signal in a -0.01 eV window about the maximum of the lowest energy moiré band of WSe$_2$ is averaged (e.g., Fig. 2a, b, Supplementary Figs. 7 and 8a). For Fig. 2a, b, these traces are then normalized for better comparison of the dynamics specifically. The overall $|\Delta R/R|$ trend (Supplementary Fig. 5) is analyzed by averaging the rectangular region about the maximum signal along both the probe energy axis (in a -0.01 eV window about the maximum of the lowest energy moiré band of WSe$_2$) and temporal dimensions (in the Δt window from 7.5 to 8.5 ps).

To isolate the dynamics from the abovementioned time traces, fits are performed. For $\nu = -1$ and -2, the normalized fits compared directly to the data are shown in Fig. 2a, b (black lines) as well as separately in Fig. 2c, d. The corresponding normalized residuals are shown in Supplementary Fig. 6. A comparison between the unnormalized fits and data for both states is shown in Supplementary Fig. 7. For $\nu = 0$, Supplementary Fig. 8a shows the fits (where applicable) in red where the corresponding residuals are shown in Supplementary Fig. 8b, c. For all fits, the coherent artifact region arising from pump-probe overlap is omitted. All errors are given by 99% confidence intervals.

The $\nu = -1$ data for pump fluence $f = 3, 7, 10$, and 14 μJ/cm^2 are fit by a biexponential function with disordering captured by the functional form $A_d \exp[t/\tau_d]$ and recovery by $A_r \exp[t/\tau_r]$. The $\nu = -1$ data for pump fluence $f = 28, 56$, and 85 μJ/cm^2 are fit using the aforementioned form with the inclusion of an additional term, $A_\infty \exp[t/\tau_\infty]$, to account for the additional component relating to thermionic emission (discussed further below). Here, $\tau_\infty = 500$ ps is fixed as the timescale for this process is beyond the duration of the present experiment and is therefore unresolvable. Figures 3–4 show the obtained time constants for disordering, τ_d, and recovery, τ_r, as a function of fluence. Supplementary Fig. 10 shows the corresponding rate of recovery, $k_r = 1/\tau_r$, as a function of fluence.

The $\nu = -2$ data for pump fluence $f = 3, 7, 10, 14, 28$, and 56 μJ/cm^2 are fit using a function with disordering captured by the functional form $A_d \exp[t/\tau_d]$ and recovery by $A_r /(1 + A_r \cdot t/\tau_{r, eff})$. As explained in the text and supported by Fig. 4 ($\tau_r/\tau_{r, eff}$ as a function of fluence) and Supplementary Fig. 10 ($k_r/k_{r, eff}$ as a function of fluence), the recovery for $\nu = -2$ is best represented by a second order process as captured by the employed functional form for recovery. Figure 3 shows the corresponding τ_d as a function of fluence. The $\nu = -2$ data for pump fluence $f = 85$ μJ/cm^2 is fit using the above form with the inclusion of an additional term, $A_\infty \exp[t/\tau_\infty]$, to account for the additional component relating to thermionic emission (discussed further below). Here, $\tau_\infty = 500$ ps is fixed as the timescale for this process is beyond the duration of the present experiment. We note that unlike $\nu = -1$, this term was not necessary for fitting the $f = 28$ and 56 μJ/cm^2 data. This is likely because the overall increased signal strength for $\nu = -2$ versus $\nu = -1$ obscures contributions from this component at $f = 28$ and 56 μJ/cm^2 in the former.

The $\nu = 0$ data for pump fluence $f = 28$, 56, and 85 μJ/cm^2 is fit using a function with rise captured by the functional form $A_{rise}\exp[t/\tau_{rise}]$ and an additional long-lived component by $A_\infty\exp[t/\tau_\infty]$. Here, $\tau_\infty = 500$ ps is again fixed as the timescale for this process is beyond the duration of the present experiment. The average $\tau_{rise} = 1.4 \pm 0.4$ ps (see Supplementary Fig. 8d). Meaningful fits were unable to be attained for $f < 28$ μJ/cm^2.

We attribute the observed dynamics for $\nu = 0$ with $f > 14$ μJ/cm^2 (as well as the presence of the additional long-lived component, τ_∞, for $\nu = -1$, -2) to hot hole injection (into the WSe$_2$/WS$_2$ bilayer) via thermionic emission following unavoidable photo-excitation of the Gr electrodes at sufficiently high excitation densities (schematically depicted in Supplementary Fig. 9)[40,41]. We note that in Supplementary Fig. 9, the shown Gr and h-BN band alignment is based on ref. 41, while the WSe$_2$ and WS$_2$ band alignment is based on ref. 49. As described in refs. 40,41, photoexcited carriers in the Gr can rapidly thermalize via scattering (e.g., Auger-like process). Following this, 'hot' carriers (specifically holes) in the tail of the resulting thermal distribution have sufficient energy to overcome the Gr/h-BN/WSe$_2$ (or Gr/h-BN/WS$_2$) energetic barrier (i.e., valence band offset) and to undergo interlayer transfer. Further, this process is highly pump fluence-dependent, as also captured clearly in the time traces of the $\nu = 0$ where dynamics are only observed for $f > 14$ μJ/cm^2. This is consistent with the additional long-lived component only being necessary in this same high fluence regime for proper fitting of the correlated state dynamics. Interlayer charge transfer ultimately driven via thermionic emission is linked to a multi-component timescale with a faster (<90 fs) and a slower (~1 ps) contribution[41]. While the former is unresolvable within our instrument response function (and is mainly related to the thermalization rather than the transfer process), the latter agrees well with the fit τ_{rise} for $\nu = 0$ as expected (and is mainly related to interlayer transfer). The long-lived component (τ_∞) in our measurement (for $\nu = 0$, -1, -2) may result from, in addition to this thermionic hole transfer and charging, transient lattice heating. This process does not interfere with the observed disordering/reordering of the $\nu = -1$, -2 states.

Data availability

The data within this paper are available upon request.

References

1. Cao, Y. et al. Correlated insulator behaviour at half-filling in magic-angle graphene superlattices. *Nature* **556**, 80–84 (2018).
2. Tang, Y. et al. Simulation of Hubbard model physics in WSe2/WS2 moiré superlattices. *Nature* **579**, 353–358 (2020).
3. Regan, E. C. et al. Mott and generalized Wigner crystal states in WSe$_2$/WS$_2$ moiré superlattices. *Nature* **579**, 359–363 (2020).
4. Wang, L. et al. Correlated electronic phases in twisted bilayer transition metal dichalcogenides. *Nat. Mater.* **19**, 861–866 (2020).
5. Shimazaki, Y. et al. Strongly correlated electrons and hybrid excitons in a moiré heterostructure. *Nature* **580**, 472–477 (2020).
6. Xu, Y. et al. Correlated insulating states at fractional fillings of moiré superlattices. *Nature* **587**, 214–218 (2020).
7. Li, H. et al. Imaging two-dimensional generalized Wigner crystals. *Nature* **597**, 650–654 (2021).
8. Liu, E. et al. Excitonic and valley-polarization signatures of fractional correlated electronic phases in a WSe2/WS2 Moiré Superlattice. *Phys. Rev. Lett.* **127**, 37402 (2021).
9. Wang, X. et al. Light-induced ferromagnetism in moiré super-lattices. *Nature* **604**, 468–473 (2022).
10. Huang, X. et al. Correlated insulating states at fractional fillings of the WS2/WSe2 moiré lattice. *Nat. Phys.* **17**, 715–719 (2021).
11. Miao, S. et al. Strong interaction between interlayer excitons and correlated electrons in WSe2/WS2 moiré superlattice. *Nat. Commun.* **12**, 3608 (2021).
12. Xu, Y. et al. A tunable bilayer Hubbard model in twisted WSe2. *Nat. Nanotechnol.* **17**, 934–939 (2022).
13. Ghiotto, A. et al. Quantum criticality in twisted transition metal dichalcogenides. *Nature* **597**, 345–349 (2021).
14. Li, T. et al. Continuous Mott transition in semiconductor moiré superlattices. *Nature* **597**, 350–354 (2021).
15. Li, T. et al. Charge-order-enhanced capacitance in semiconductor moiré superlattices. *Nat. Nanotechnol.* **16**, 1068–1072 (2021).
16. Park, H. et al. Dipole ladders with large Hubbard interaction in a moiré exciton lattice. *Nat. Phys.* **19**, 1286–1292 (2023).
17. Gao, B. et al. Excitonic Mott insulator in a Bose-Fermi-Hubbard system of moiré WS2/WSe2 heterobilayer. *Nat. Commun.* **15**, 2305 (2024).
18. Xiong, R. et al. Correlated insulator of excitons in WSe 2 /WS 2 moiré superlattices. *Science* **380**, 860–864 (2023).
19. Cao, Y. et al. Unconventional superconductivity in magic-angle graphene superlattices. *Nature* **556**, 43–50 (2018).
20. Lu, X. et al. Superconductors, orbital magnets and correlated states in magic-angle bilayer graphene. *Nature* **574**, 653–657 (2019).
21. Sharpe, A. L. et al. Emergent ferromagnetism near three-quarters filling in twisted bilayer graphene. *Science* **365**, 605–608 (2019).
22. Chen, G. et al. Tunable correlated Chern insulator and ferro-magnetism in a moiré superlattice. *Nature* **579**, 56–61 (2020).
23. Serlin, M. et al. Intrinsic quantized anomalous Hall effect in a moiré heterostructure. *Science* **367**, 900–903 (2020).
24. Li, T. et al. Quantum anomalous Hall effect from intertwined moiré bands. *Nature* **600**, 641–646 (2021).
25. Cai, J. et al. Signatures of fractional quantum anomalous Hall states in twisted MoTe2. *Nature* **622**, 63–68 (2023).
26. Park, H. et al. Observation of fractionally quantized anomalous Hall effect. *Nature* **622**, 74–79 (2023).
27. Zeng, Y. et al. Thermodynamic evidence of fractional Chern insu-lator in moiré MoTe2. *Nature* **622**, 69–73 (2023).
28. Lu, Z. et al. Fractional quantum anomalous Hall effect in multilayer graphene. *Nature* **626**, 759–764 (2024).
29. Hubbard, J. Electron correlations in narrow energy bands. *Proc. R. Soc. Lond. A* **276**, 238–257 (1963).
30. Quintanilla, J. & Hooley, C. The strong-correlations puzzle. *Phys. World* **22**, 32–37 (2009).
31. Arsenault, E. A. et al. Two-dimensional Moiré polaronic electron crystals. *Phys. Rev. Lett.* **132**, 126501 (2024).
32. Zhang, Y., Yuan, N. F. Q. & Fu, L. Moiré quantum chemistry: charge transfer in transition metal dichalcogenide superlattices. *Phys. Rev. B* **102**, 201115 (2020).
33. Yuan, L. et al. Twist-angle-dependent interlayer exciton diffusion in WS2–WSe2 heterobilayers. *Nat. Mater.* **19**, 617–623 (2020).
34. Wu, F., Lovorn, T., Tutuc, E. & Macdonald, A. H. Hubbard model physics in transition metal dichalcogenide Moiré bands. *Phys. Rev. Lett.* **121**, 26402 (2018).
35. Murakami, Y., Golež, D., Eckstein, M. & Werner, P. Photo-induced nonequilibrium states in Mott insulators. *arXiv preprint arXiv:2310.05201* (2023).
36. Hellmann, S. et al. Time-domain classification of charge-density-wave insulators. *Nat. Commun.* **3**, 1069 (2012).
37. Petek, H. & Ogawa, S. Femtosecond time-resolved two-photon photoemission studies of electron dynamics in metals. *Prog. Surf. Sci.* **56**, 239–310 (1997).
38. Ung, S. F., Lee, J. & Reichman, D. R. Competing generalized Wigner crystal states in moiré heterostructures. *Phys. Rev. B* **108**, 245113 (2023).
39. Matty, M. & Kim, E.-A. Melting of generalized Wigner crystals in transition metal dichalcogenide heterobilayer Moiré systems. *Nat. Commun.* **13**, 7098 (2022).

40. Rodriguez-Nieva, J. F., Dresselhaus, M. S. & Levitov, L. S. Thermionic emission and negative dI/dV in photoactive graphene hetero-structures. *Nano Lett.* **15**, 1451–1456 (2015).
41. Ma, Q. et al. Tuning ultrafast electron thermalization pathways in a van der Waals heterostructure. *Nat. Phys.* **12**, 455–459 (2016).
42. Li, Y. et al. Coherent modulation of two-dimensional Moiré states with On-Chip THz Waves. *Nano Lett.* **24**, 12156–12162 (2024).
43. Rohwer, T. et al. Collapse of long-range charge order tracked by time-resolved photoemission at high momenta. *Nature* **471**, 490–494 (2011).
44. Rossnagel, K. On the origin of charge-density waves in select layered transition-metal dichalcogenides. *J. Phys: Condens Matter* **23**, 213001 (2011).
45. Liu, L. et al. Direct identification of Mott Hubbard band pattern beyond charge density wave superlattice in monolayer 1T-NbSe2. *Nat. Commun.* **12**, 1978 (2021).
46. Papaj, M. & Lewandowski, C. Probing correlated states with plas-mons. *Sci. Adv.* **9**, eadg3262 (2023).
47. Clarke, D. G. Particle-hole bound states in Mott-Hubbard insulators. *Phys. Rev. B* **48**, 7520–7525 (1993).
48. Wang, J. et al. Diffusivity reveals three distinct phases of interlayer excitons in MoSe2/WSe2 Heterobilayers. *Phys. Rev. Lett.* **126**, 106804 (2021).
49. Zhang, C. et al. Systematic study of electronic structure and band alignment of monolayer transition metal dichalcogenides in Van der Waals heterostructures. *2d Mater.* **4**, 015026 (2017).

Author contributions

E.A.A., Y.L., and X.Y.Z. conceived this work. E.A.A. and Y.L. carried out all spectroscopic measurements. B.Y. was responsible for sample fabrication and characterization, under the supervision of C.R.D. T.T. and K.W. provided the h-BN crystal. J.C.H. provided the WSe$_2$ crystal. E.A.A. and X.Y.Z. interpreted the results, with input from X.X. The manuscript was prepared by E.A.A. and X.Y.Z. in consultation with all other authors. X.Y.Z. supervised the project. All authors read and commented on the manuscript.

Competing interests

The authors declare no competing interests.

Additional information

Supplementary information The online version contains supplementary material available at https://doi.org/10.1038/s41467-024-54886-8.

Correspondence and requests for materials should be addressed to X.-Y. Zhu.

Peer review information *Nature Communications* thanks Jacek Majewski, Su-Fei Shi, and the other, anonymous, reviewer for their contribution to the peer review of this work. A peer review file is available.

Reprints and permissions information is available at http://www.nature.com/reprints

Publisher's note Springer Nature remains neutral with regard to jurisdictional claims in published maps and institutional affiliations.